DOI: 10.1002/ejic.200800987

A Study of the Influence of Composition on the Microstructural Properties of ZnO/Al_2O_3 Mixed Oxides[‡]

Shaojun Miao,[a] Raoul Naumann d'Alnoncourt,*[a] Thomas Reinecke,[b] Igor Kasatkin,[c] Malte Behrens,[c] Robert Schlögl,[c] and Martin Muhler[a]

Keywords: Zinc / Aluminum / Coprecipitation / Heterogeneous catalysis

A series of ZnO/Al_2O_3 mixed oxide samples with varying Zn/Al ratio is prepared by coprecipitation, ageing, drying, and calcination. Samples are investigated in the state after drying and calcination. The applied methods include X-ray diffraction, solid-state ^{27}Al magic-angle spinning nuclear magnetic resonance spectroscopy, transmission electron microscopy and thermogravimetric experiments coupled with evolved gas analysis. Phases present in the dried precursor samples include hydrozincite, zaccagnaite, and an unknown phase. After calcination zinc oxide and spinel can be found. All results indicate the substitution of Al ions for Zn ions in zinc oxide of zinc-rich samples.

Introduction

ZnO-based materials are of extraordinary importance and a substantial number of papers have been published on synthesis and properties of ZnO materials.[1,2] Zincite, ZnO, stable over a wide range of pressure-temperature conditions is used as a catalyst support, gas sensor, UV-light emitter, ceramic varistor, surface acoustic wave device, and piezoelectric transducer. Because of the importance of methanol as a basic chemical the role of ZnO as a component of industrially used catalysts for methanol synthesis (Cu/ZnO/Al_2O_3) is of particular interest.[3–8] It is widely accepted that although copper is the active site for the synthesis of methanol zincite and defects in zincite have a major influence on catalyst activity.[2,9] Existing models and recent theoretical calculations of methanol synthesis over pure zincite suggest that oxygen vacancies formed on the surface of zincite crystals may be active sites for CO (and CO_2) chemisorption under methanol synthesis conditions.[4,7,10–14]

In order to control the functional properties of materials it is necessary to govern not only their composition and morphology but also their defect structure.[15–18] To understand and ultimately control the defect content of inorganic nanostructures can be seen as an important goal. Zincite is of particular importance due to its oxygen defects that lead to deviations in the zinc/oxygen ratio ($ZnO_{0.99993}$ at 1073 K).[19] Empty oxygen sites (oxygen vacancies, V_O^{2+}) are potential wells that can trap either one (V_O^{+}) or two (V_O^{0}) electrons.[20] The occurrence of interstitial zinc atoms is also known.

Extrinsic defects in bulk zincite involve the substitution of zinc for heteroatoms.[21] Intrinsically, zincite is a wide-bandgap n-type semiconductor with a bandgap energy E_g = 3.37 eV.[2] Substitution of divalent ions for Zn has been studied with respect to bandgap variation. The introduction of trivalent ions, for example Al, Ga, or In, allows variation of the concentration of free charge carriers, by producing donor or acceptor levels.[22–25] It can be speculated that Al functions not only as a structural promoter in the industrial catalyst system used for methanol synthesis. The incorporation of Al atoms into zincite may change the electronic properties of zincite and thus the properties of metallic Cu supported on zincite.

In the case of the binary catalyst system Cu/ZnO, detailed studies concerning the phases formed during the preparation steps of coprecipitation, ageing, and drying are found in the literature.[26,27] The identified phases include hydrozincite, aurichalcite, and rosasite. The phase composition of the precursor materials varied with the Cu/Zn molar ratio and the preparation conditions. The microstructural properties and the catalytic activities for synthesis of methanol of the mixed oxide samples obtained by calcination were correlated to the phases present during the preparation. This correlation was described as the chemical memory of the phases.[26]

In the present contribution the influence of the composition, i.e. the molar ratio of zinc and aluminum, on the microstructural properties of ZnO/Al_2O_3 mixed oxide samples is studied. The samples are prepared via coprecipitation from a solution of the metal nitrates using a solution of

---

[‡] Coprecipitated samples, I.

[a] Laboratory of Industrial Chemistry, Ruhr University Bochum, 44780 Bochum, Germany
E-mail: naumann@fhi-berlin.mpg.de
[b] Institute of Geology, Mineralogy & Geophysics, Ruhr-University Bochum
44780 Bochum, Germany
[c] Fritz-Haber-Institut der Max-Planck-Gesellschaft, Department of Inorganic Chemistry,
14195 Berlin, Germany

sodium carbonate as the precipitating agent. The preparation follows a standardized procedure under controlled conditions (e.g. pH, temperature, stirring speed, reaction and ageing time) that was previously used for the preparation of copper catalysts.[28–31] A detailed description of the coprecipitation procedure is given in ref.[26]. The coprecipitation is followed by the steps of washing, drying, and calcination. The final product is a mixed oxide with a sodium content low enough for catalytic applications.[32] For a correlation of the sample properties to single phases formed during coprecipitation, ageing and drying, the dried, yet not calcined precursor materials are included in the investigations.

Please note that the conditions applied during preparation are chosen from the point of view of catalysis research. Materials used in catalysis seldom consist of large well-ordered crystallites that can be easily characterized. More often catalytically relevant materials contain small, defective, and irregular nanoparticles as the active compound. Therefore, part of the results presented in this contribution, e.g. X-ray diffractograms, necessarily cannot meet the quality of results that are obtained for pure, well-crystallized synthetic compounds.

The label of the samples indicates the nominal Zn content and the state of the sample. The extension -d refers to the precursor material obtained after drying of the precipitate, while -c refers to calcined mixed oxide samples. For example, Zn55-d is a precursor material with a molar Zn/Al ratio of 55:45.

Results and Discussion

Calcined Mixed Oxide Samples

Samples of the mixed oxides obtained by calcination of the dried precursor materials are investigated by X-ray diffraction, solid-state ^{27}Al magic-angle spinning nuclear magnetic resonance spectroscopy (^{27}Al MAS NMR), static nitrogen physisorption experiments (BET), and transmission electron microscopy.

The XRD patterns of the calcined samples are compared in Figure 1. The data of two Powder Diffraction Files (PDF) provided by the International Center for Diffraction Data (ICDD) and assigned to zincite, ZnO (hexagonal wurtzite structure) and the zinc aluminum spinel gahnite, $ZnAl_2O_4$ (36–1451 and 05–669, respectively) are included for comparison. All reflections can be assigned to either zincite or ZnAl-spinel. Samples with a zinc content higher than 55% contain only zincite as detectable phase. Samples with a zinc content of 40 and 55% contain both phases, with less zincite being present in Zn40-c than in Zn55-c. In sample Zn20-c a very minor amount of zincite is detected in addition to ZnAl-spinel. The Zn-free sample Zn00-c is nearly X-ray amorphous, the broad and weak reflections in its diffractogram can be assigned to various transition aluminas, e.g. γ-, δ-, or θ-alumina.

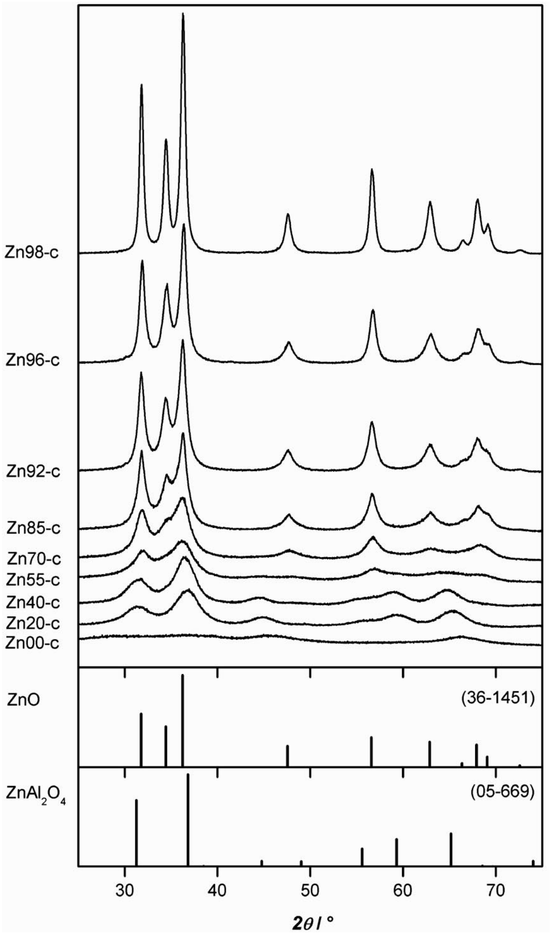

Figure 1. X-ray diffractograms of mixed oxide samples in the state after calcination. Patterns of zincite, ZnO (hexagonal wurtzite structure, PDF 36–1451) and cubic ZnAl-spinel, $ZnAl_2O_4$ (PDF 05–669) are included for comparison.

The crystallite size of zincite and ZnAl-spinel nanoparticles reported in Table 1 is calculated from the integral breadth of the (100) reflection of zincite and the (311) reflection of spinel, based on the assumption of a monodisperse distribution and spherical shape of the crystallites. Although the absolute size values have to be considered as estimates, the relative changes with composition appear to be reliable (for a detailed discussion of the shape and size of zincite crystallites in Zn-rich samples, see below). In samples Zn55-c to Zn00-c the crystallite size could be assessed for ZnAl-spinel (in part) but not for zincite and alumina phases, because of the strong peak overlap and the minor bulk content of zincite, respectively the unclear phase assignment in Zn00-c.

In the Zn-rich part of the binary system (Zn100-c to Zn70-c) the estimated mean crystallite size of zincite decreases from 16 nm to about 5 nm, except for a reversal at Zn98-c (see Figure 2). The trend is inversely correlated with the specific surface area (BET), which ranges from 30 $m^2 g^{-1}$ to 116 $m^2 g^{-1}$, with a minimum at Zn98-c corresponding to the crystallite size reversal. In the Al-rich part of the system the Zn-free sample (Zn00-c) has the highest specific surface

Table 1. Composition and properties of calcined mixed oxide samples.[a]

Sample	Phases	BET [$m^2 g^{-1}$]	a [nm]	c [nm]	V [nm^3]	$\bar{e}_{(hk0)}$ (10^{-3})	$\bar{e}_{(00l)}$ (10^{-3})	$<D_{(hk0)}>$ [nm]	$<D_{(00l)}>$ [nm]	$<D>$ [nm]
Zn100-c	zincite	39	0.32496(3)	0.52089(9)	0.04763(1)	2.6	2.2	16.6	17.0	16
Zn98-c	zincite	30	0.32475(5)	0.5209(1)	0.04757(2)	2.2	<1.0	17.5	11.6	17
Zn96-c	zincite	44	0.32460(5)	0.5208(1)	0.04752(2)	3.1	n. d.[b]	11.9	8.5	12
Zn92-c	zincite	66	0.32455(8)	0.5203(2)	0.04746(3)					10
Zn85-c	zincite	98								8
Zn70-c	zincite	116								≈5
Zn55-c	zincite ZnAl-spinel	193	0.8116(2)							
Zn40-c	ZnAl-spinel minor zincite	130	0.81435(5)							≈3
Zn20-c	ZnAl-spinel zincite?	215	0.80937(5)							≈2
Zn00-c	various aluminas	268								

[a] Phases gives a list of phases detectable by XRD; BET gives the specific surface area of the samples measured by N_2 physisorption after degassing for 2 h under dynamic vacuum conditions at 473 K; a and c are the lattice parameters of the crystallographic unit cell of zincite and spinel (only a, Zn55-c, Zn40-c, Zn20-c), respectively; V is the volume of the crystallographic unit cell; $\bar{e}_{(hk0)}$ is the root mean-square strain perpendicular to the c axis in zincite crystallites; $\bar{e}_{(00l)}$ is the root mean-square strain parallel to the c axis in zincite crystallites; $<D_{(hk0)}>$ is the mean diameter of the prism base of zincite crystallites; $<D_{(00l)}>$ is the mean length of the prismatic zincite crystallites; $<D>$ is the mean crystallite size calculated with the Scherrer formula from the integral breadth of the (100) reflection in case of zincite and of the (311) reflection in case of spinel (Zn40-c, Zn20-c); values in parentheses refer to 1 sigma error. [b] Weak lattice strain could not be calculated due to the very weak and broad (004) and (006) diffraction lines.

area (268 $m^2 g^{-1}$). In specimens containing ZnAl-spinel the specific surface area first decreases from 215 $m^2 g^{-1}$ to 130 $m^2 g^{-1}$ (Zn20-c, Zn40-c) and then increases to 193 $m^2 g^{-1}$ (Zn55-c).

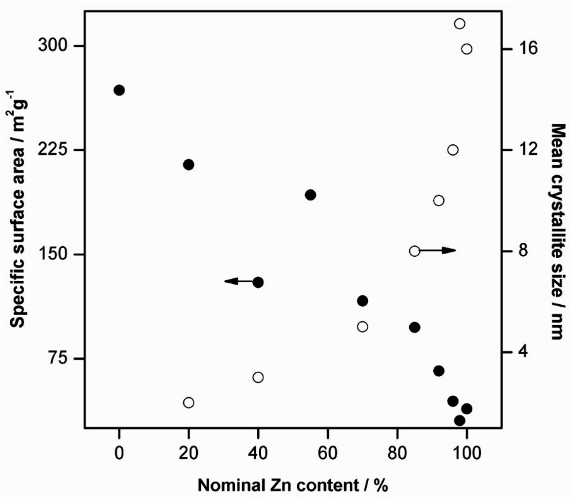

Figure 2. Specific surface area of mixed oxides and mean crystallite size of zincite (samples Zn100-c to Zn70-c) and ZnAl-spinel (samples Zn20-c and Zn40-c) as a function of nominal Zn content.

Lattice parameters of zincite in the Zn-rich samples Zn100-c, Zn98-c, Zn96-c, and Zn92-c are listed in Table 1 and displayed in Figure 3 as a function of the molar Al content. Lattice parameters of zincite in samples with nominal Al-content higher than 8 % (i.e. Zn85-c and Zn70-c) are not determined because diffraction peaks of zincite at values of 2θ>40° are extremely broad and weak and line fits at the peaks involve large errors in diffraction angles. The lattice parameters of pure nanocrystalline zincite (Zn100-c) are identical within three standard deviations with those of well-crystallized zincite [PDF 36–1451, a = 0.324982(9) nm, c = 0.520661(15) nm, at ca. 299 K] and of nanocrystalline zincite [a = 0.324988(5) nm, c = 0.520743(9) nm, at 294 K], formed by thermal decomposition of zinc oxalate.[33] Lattice parameters of zincite decrease with increasing Al, respectively decreasing Zn content (see Figure 3). Substitution of the smaller Al^{3+} ion (ionic radius 0.039 nm[34]) for the Zn^{2+} ion (ionic radius+ 0.060 nm[55]) in the tetrahedral cation site of zincite may be responsible for the decrease of the unit cell dimensions. At first, our data suggest a nonlinear behavior of a and c with composition. However, this should be looked at cautiously, because errors are large relative to the changes in the lattice parameters. Applying 2σ or 3σ errors, the data follow an overall linear relationship.

Al-incorporation in zincite is well known concerning the use of zincite as a semiconductor (AZO, Al-doped zinc oxide). On the ZnO-Al_2O_3 binary, zincite coexists with gahnite, $ZnAl_2O_4$, up to the eutectic at ca. 1968 K in air.[35,36] At the eutectic Al solubility in zincite is at a maximum of 9.4 mol-% that gradually decreases to <0.5 mol-% at $T \leq$ 1673 K.[35] Lattice substitution of Al^{3+} for Zn^{2+} and charge balance in zincite, $Zn_{1-1.5x}Al_xO$, is likely to be accomplished by the simultaneous introduction of cation vacancies. Alternatively, Al^{3+} may reside in octahedral and/or tetrahedral interstitial sites of the zincite lattice.[22]

In a recent study on the synthesis and local structure of Al-, Ga-, and In-doped zincite prepared by chemical vapor synthesis (CVS) at 1273 K Brehm et al. found that the lattice parameter c of zincite decreases and a, b increases with the incorporation of 2 and 5 at% Al^{3+}.[22] The net effect of Al-incorporation on the unit cell volume of zincite is undetectable within error limits. The increase in a, b and the marked decrease in c are in contrast with our results.

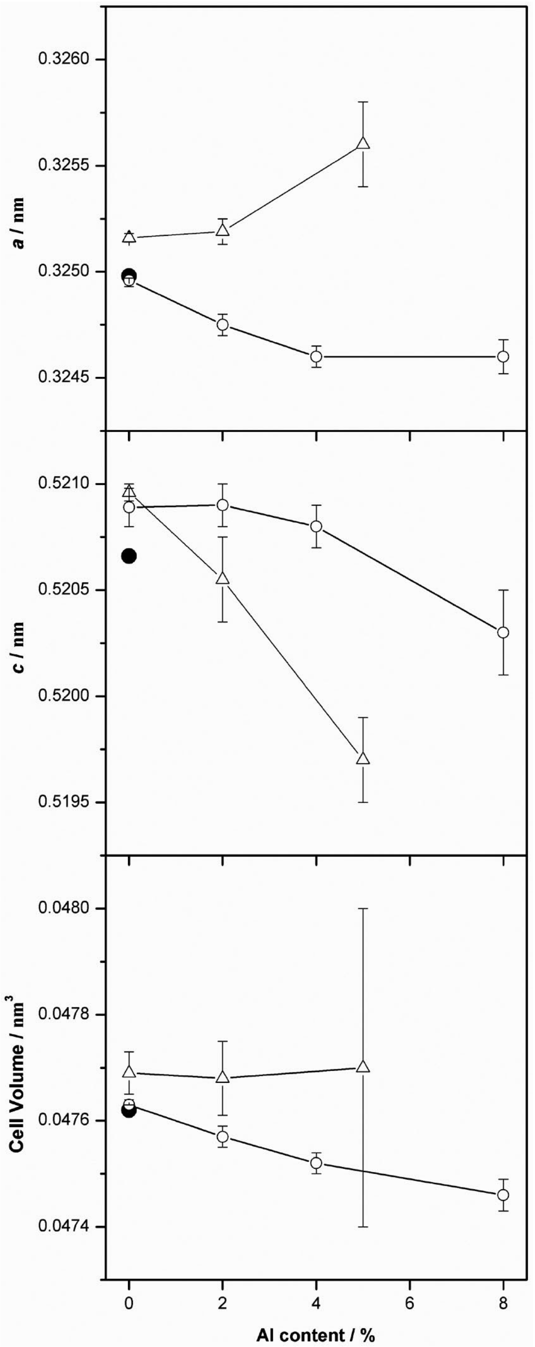

Figure 3. Unit cell parameters *a* and *c*, and unit cell volume *V* of zincite in calcined mixed oxide samples as a function of nominal Al content (hollow circles). The lattice parameters of pure zincite taken from PDF 36–1451 (filled circles) reasonably agree with the parameters of Zn100-c. Unit cell parameters of CVS zincite, containing 0, 2, and 5 mol-% Al, reported in ref.[22] are shown for comparison (hollow triangles). Bars indicate ±1 sigma error of lattice parameters.

The estimated mean crystallite size of the samples in ref.[22] ranges from 25 nm (pure ZnO) to 11 nm (ZnO with 5 at.% Al) and is thus almost identical with our specimens (17–12 nm; Table 1). From the analysis of Al backscattering in Zn EXAFS experiments Brehm et al. argue for the presence of Al in six-coordinate interstitial sites rather than in tetrahedral Zn lattice sites of CVS zincite. The distinct evolution of lattice parameters with increasing Al content in our samples suggests a different mechanism of Al incorporation, i.e. substitution in tetrahedrally coordinated lattice sites. If Al^{3+} were present in the small four-coordinate Zn(3)-site of the precursor hydrozincite, $Zn_5(OH)_6(CO_3)_2$,[37] which occurs in Zn-rich samples (see below), the collapse of the hydrozincite structure during calcination may possibly favor the incorporation of Al^{3+} in the Zn-site of zincite.

Another reason for uncertainty in the lattice parameters should be discussed in this context. While refining their values from full-pattern Rietveld fits, Brehm et al. possibly did not consider angular shifts due to geometrical aberrations (e.g. sample height error, flat specimen error) inherent in the Bragg–Brentano diffraction geometry. During the refinement process these may propagate into the lattice parameters. As sample height errors are commonly slightly different in a set of measurements, inconsistencies in lattice parameters between different data sets may arise. In our experience such errors can be avoided and better consistency can be achieved by use of an internal line standard and by coupling the geometric constraints between the standard and the investigated phases in the refinement.

The cubic lattice parameter *a* of Zn-Al-spinel in Zn20-c, Zn40-c, and Zn55-c (Table 1) is significantly higher than that of gahnite, $^{IV}(Zn_{1-x}Al_x)^{VI}(Al_{2-x}Zn_x)O_4$, with normal cation distribution [$a = 0.80865(1)$ nm at $x = 0.01$, PDF 82–1534[38]]. There are different possible explanations for an increase in the lattice parameter of synthetic ZnAl-spinels compared with their well-ordered end-member composition. The inversion parameter x of gahnite, varying from ca. 0.01 at $T = 1173$ K to 0.05 at $T = 1573$ K, is associated with a linear increase of lattice parameter *a* from 0.8086 nm to 0.8088 nm.[38] In the normal spinel $MgAl_2O_4$, a high dislocation density induced by irradiation with high-energy Ar^+ ions has the effect of an increasing lattice parameter (compared with the same composition containing few lattice defects).[39] A similar behavior is expected for gahnite. At very small crystal size (<20 nm) the lattice parameters of ionic solids expand because the increased surface-to-volume ratio changes the balance between the long-range Coulomb force and the short-range repulsive interactions.[40] In the absence of microstructural and size-dependent investigations we cannot distinguish between the possible effects of cation disorder, dislocations and very small crystal size on the lattice parameter of ZnAl-spinel in the calcined samples.

Crystallite size and strain of nanocrystalline zincite synthesized from various precursor phases (e.g. zinc oxalate, zinc hydroxy nitrate, zinc hydroxy carbonate, and zinc acetate) has been extensively investigated.[33,41–43] These studies provide the basis for the interpretation of our data. For line-broadening analysis, the integral breadths β_f of the zincite diffraction lines in Zn96-c, Zn98-c, and Zn100-c are converted to reciprocal units β_f^* [$\beta_f^* = \pi\beta_f\cos\theta/(180\lambda)$, in nm^{-1} units] and plotted against d^*, the reciprocal distance of the lattice planes (Williamson–Hall plot). Two such plots are shown for Zn100-c (Figure 4, a) and Zn98-c (Figure 4, b). The pattern of Zn96-c is very similar to Zn98-c and the inferences drawn from Zn98-c are valid also for Zn96-c.

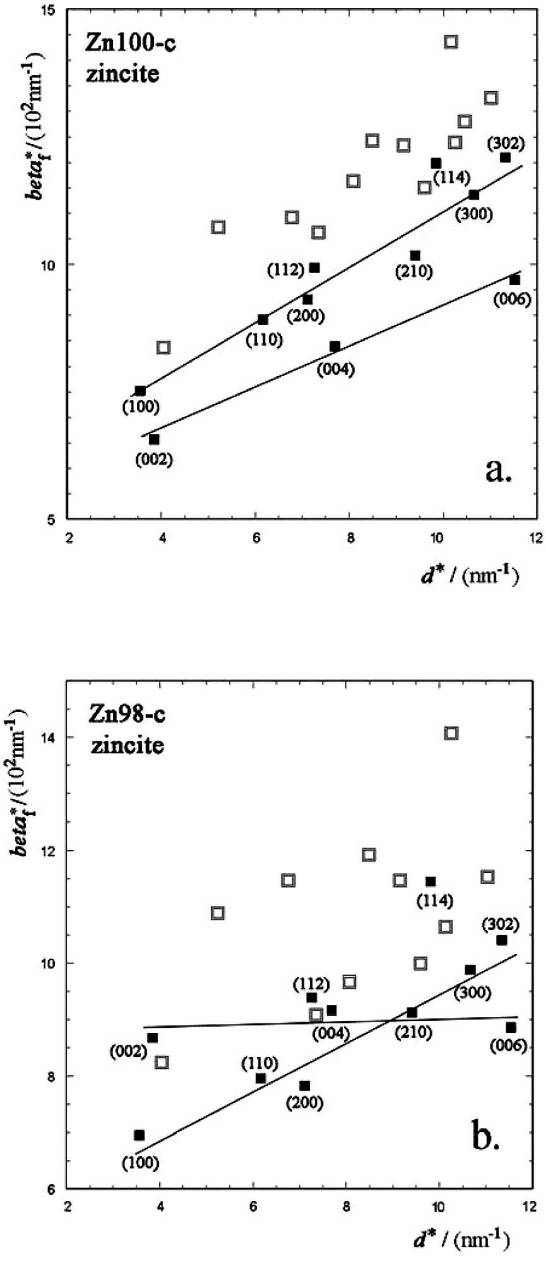

Figure 4. Williamson–Hall plots showing β_f^* [$= \pi\beta_f\cos\theta/(180\lambda)$] vs. reciprocal lattice distance d^* of diffraction lines measured in Zn100-c and Zn98-c. Diffraction lines broadened by small size and microstrain are shown with black squares and are labeled with their Miller indices. Diffraction lines broadened by size, strain, and stacking disorder (open squares) are unlabeled. Straight lines indicate the slope of (*hk*0) and (00*l*) diffraction lines, respectively.

The Williamson–Hall plot of Zn100-c (Figure 4, a) shows significant scatter in β_f^* of the diffraction lines. These can be grouped as follows. For a given value of d^*, (*hk*0) or (*hkl*) reflections with *l* even and *h*-*k* = 3n [i.e. (100), (002), (110), (200), (004) etc.] have lower values of β_f^* than those with *h*-*k* = 3n ± 1, *l* odd [e.g. (101), (103), (201), (203), (211), (105)] and *h*-*k* = 3n ± 1, *l* even [e.g. (102), (202), (104), (212), (204)]. Line broadening of the latter two groups of reflections is due to hexagonal stacking faults.[33] The first group is unaffected by stacking faults and their integral breadths only result from size and strain broadening. It is obvious from Figure 4 (a) that (*h*00) and (*hk*0) reflections plot on or close to a straight line with positive slope which is different from the straight line with the (00*l*) reflections. The different intercepts of the lines indicate a minor shape anisotropy, i.e. the column lengths of the (*h*00) and (*hk*0) lattice planes are almost identical, and slightly shorter than the column length of the (00*l*) reflections. As zincite often crystallizes as hexagonal prisms, the shape anisotropy can be visualized as due to a longer diameter of the prism axis (the crystallographic *c* direction) relative to equal diameters of the prism basis (corresponding to the *a* and *b* directions).

The increase of β_f^* with d^* indicates a contribution to line broadening by microstrain in the *c* as well as the *a*-*b* lattice directions. To separate the effects of size and strain, the β_f^* and d^* values of the (100), (110), (200), (210), and (300) respectively the (002), (004), and (006) reflections are converted to average size-strain plots to solve for the slope ($1/\varepsilon_\beta$) and the intercept $(\eta/2)^2$ in the equation $(\beta_f^*/d^*)^2 = \varepsilon_\beta^{-1}\,\beta_f^*/(d^*)^2 + (\eta/2)^2$, where ε_β is the mean apparent diameter and η is the mean strain.[41] Assuming the root mean-square strain (rms strain) description appropriate for the strain broadening (for definition, see ref.[44]), an rms strain of $\bar{e} = 2.2\times10^{-3}$ is calculated for the lattice direction parallel to the prism axis (*c* axis) and $\bar{e} = 2.6\times10^{-3}$ perpendicular to it.

The values of the mean apparent size ε_β are 14.7 nm for the *a*-*b* direction and 17.0 nm for the *c* direction. If a prismatic hexagonal shape of the crystallites is assumed,[42,43] the mean length of the prism is $<D_{(00l)}> = \varepsilon_{\beta((00l)} = 17.0$ nm and the mean diameter of the prism basis is $<D_{(hk0)}> = K_{\beta(hk0)}\varepsilon_{\beta(hk0)} = 16.6$ nm (Scherrer constant $K_{\beta(hk0)} = 1.125$[45]). Zincite crystallites in Zn100-c are thus almost isometric in shape. The same property has been observed in zincite synthesized by low-temperature decomposition of commercial zinc hydroxy carbonate.[42]

Previous studies indicate the presence of microstrain in nanocrystalline zincite obtained by low-temperature (110–160 °C) calcination of zinc acetate[42] or zinc hydroxy nitrate,[46] and by room-temperature precipitation from the reaction of β-Zn(OH)Cl or $Zn_5(OH)_8Cl_2{\cdot}H_2O$ precursors with *n*-buthylamine.[47] Notably, the rms microstrain has the same magnitude ($\bar{e} = 0.1$–4.9×10^{-3}) and the anisotropy [$\bar{e}_{(hk0)} > \bar{e}_{(00l)}$] has the same order as in our sample. Microstrain is not observed in zincite samples made by thermal decomposition of zinc hydroxy carbonate,[42] zinc oxalate,[33] and zinc hydroxy nitrate,[46] though stacking disorder is detected in most of these samples. A simple relationship between synthesis conditions (e.g. temperature, heating rate, precursor) and the presence or absence of microstrain in zincite is not apparent.

We also investigated chemically pure, nanocrystalline (ca. 60 nm) zincite (NanoTek® zinc oxide, product code 1701) produced by high-temperature CVS. Unlike the Zn100-c zincite, line broadening due to stacking disorder or microstrain is not observed in the CVS zincite. Low-temperature decomposition of the hydroxy carbonate precursor (Zn100-d) obviously introduces abundant defects in zincite, while high-temperature synthesis from the gas phase results in crystallites with largely undisturbed lattice.

The Williamson–Hall plots of Al-bearing zincites Zn98-c (Figure 4, b) and Zn96-c indicate the presence of hexagonal stacking faults, shape anisotropy, and microstrain in the *a-b* direction, but none or very low microstrain in the *c* direction. With increasing Al substitution for Zn, the mean diameter of the crystallites decreases more strongly in *c* than in *a* and *b* (Table 1), leading to a clear shape anisotropy (i.e. platy morphology). In contrast to pure zincite, Al-bearing zincites Zn98-c and Zn96-c reveal a strong anisotropy of the microstrain (Table 1). While strains in the *a-b* lattice direction are similar in all samples, the (00*l*) lattice strain decays in Al-bearing zincite.

The results of the ^{27}Al MAS NMR experiments are shown in Figure 5. Generally, three differently coordinated Al species are found in γ-Al_2O_3. Octahedrally, pentahedrally, and tetrahedrally coordinated Al can be assigned to peaks in ^{27}Al MAS NMR experiments at chemical shifts in the range of δ = –20 to 20 ppm, 25–40 ppm, and 45–80 ppm, respectively.[48–51] Correspondingly three Al species are detected in the pure Al_2O_3 sample Zn00-c with peaks at chemical shifts of δ = 8 ppm, 36 ppm, and 67 ppm. To a varying extent, these three Al species can be found in the spectra of all investigated samples. The presence of zinc in the samples leads to the formation of additional Al species. The influence of zinc on the NMR signal of octahedrally coordinated Al species is less pronounced than the effect observed in the range assignable to tetrahedrally coordinated Al species. In the range assignable to octahedrally coordinated Al, only one peak is observed in the case of all samples. However, this peak is so broad, that it is not clear whether the peak originates from one single Al species in an ill-defined surrounding or whether several different Al species contribute to this peak. With increasing zinc content the peak maximum shifts from δ = 8 ppm to about 11 ppm and back again to 6 ppm. The existence of additional octahedrally coordinated Al species can be rationalized by the presence of $ZnAl_2O_4$. In normal synthetic spinel only Zn atoms are coordinated tetrahedrally, while all Al atoms are coordinated octahedrally. Samples with low to medium zinc content (Zn20-c, Zn40-c, Zn55-c) contain significant amounts of crystalline spinel. The peak maximum correlated to octahedrally coordinated Al species in these samples is shifted towards low field compared to Zn00-c. The fact that the peak correlated to the octahedral species in sample Zn70-c is also shifted towards low field may indicate the presence of X-ray amorphous spinel. In addition, a new tetrahedrally coordinated Al species with a peak maximum at δ = 78 ppm can be found in the spinel-containing samples. The presence of this Al species indicates that the spinel formed under the applied conditions is either a partially inversed spinel or a zinc-deficient spinel of the nominal composition $Zn_{1-3x}Al_{2+2x}O_4$ in which tetrahedrally coordinated Al is partly substituted for Zn. It is found in the literature that a preparation route via coprecipitation and moderate calcination usually leads to zinc-deficient spinel[52–54] with lowered lattice parameters compared to normal spinel.[54] Partial inversion of ZnAl-spinel is usually expected to occur only at elevated temperatures not applied in our study. However, the lattice parameters calculated for spinel in Zn55-c, Zn40-c, and Zn20-c indicate no cation-deficient composition. Tetrahedrally coordinated Al species different from those found in pure alumina exist also in spinel-free samples with a high zinc content. Two new signals correlated to tetrahedral Al are found at shifts of δ = 82 ppm and δ = 48 ppm. While the signal at δ = 48 ppm is weak and broad, the signal at δ = 82 ppm is very narrow. The latter peak is the only significant peak in the spectrum of Zn96-c. Its intensity decreases with decreasing zinc content. The peak is only a very weak shoulder in the spectrum of Zn70-c and cannot be found at all in the spectrum of Zn55-c. The narrow peak form indicates that the corresponding Al species is positioned in a very well-defined surrounding. A possible explanation that fits perfectly to the XRD results described above is the substitution of Al^{3+} ions for the tetrahedrally coordinated Zn^{2+} ions in zincite.

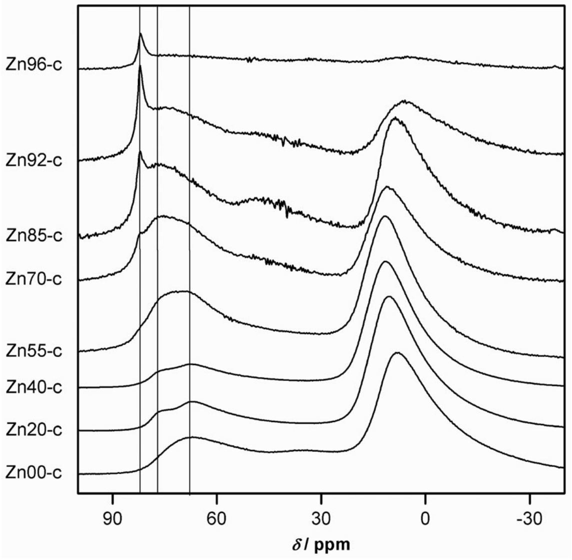

Figure 5. ^{27}Al MAS NMR spectra of mixed oxide samples in the state after calcination. Three different tetrahedrally coordinated Al-species can be assigned to peaks with maxima at δ = 82, 78, and 67 ppm.

An investigation of the samples by TEM supports the results of XRD and BET experiments. The zinc-free alumina sample Zn00-c is almost amorphous as found by XRD. Only in images of highest magnification can some areas with lattice distances typical for γ-alumina be found (see parts a and b of Figure 6). In images of the XRD-pure zincite sample Zn100-c only large agglomerates (several hundreds of nm) of small zincite crystals (several tens of nm) can be found (see parts c and d of Figure 6). Although the size of the zincite crystals is in agreement with the mean size derived from the XRD data, the shape of the crystals is rather more rod-like than isometric. These differences

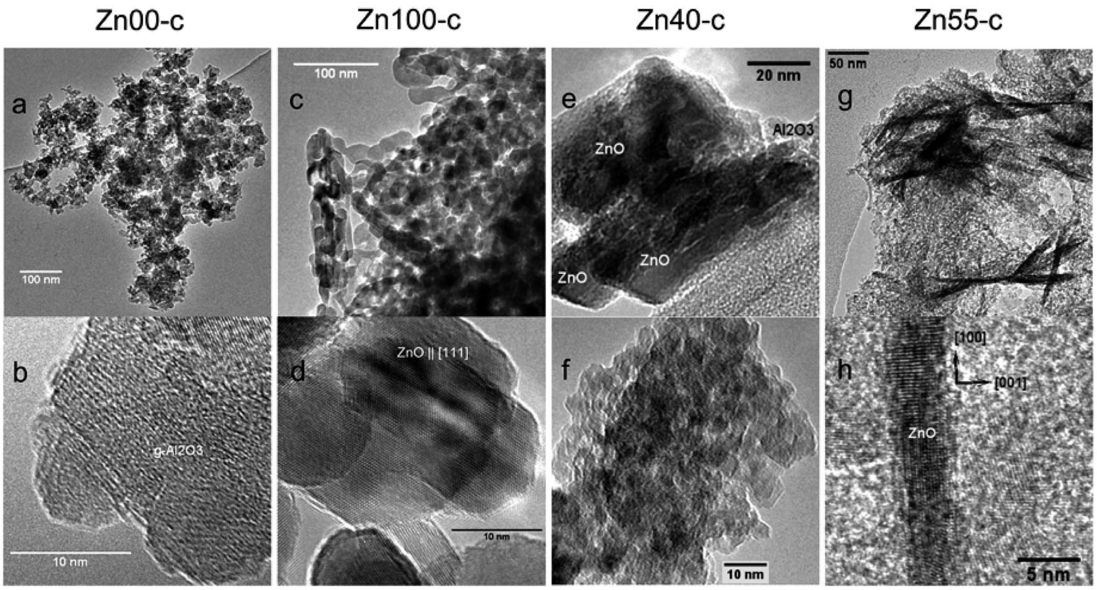

Figure 6. TEM images of mixed oxide samples in the state after calcination. The presented images are representative for the general microstructure of the corresponding sample.

might be due to the fact that the mean size derived from XRD data is related to the mean domain size and not the mean size of primary particles. The specific surface areas measured for Zn100-c and Zn00-c are in full agreement with the TEM results. The BET results obtained for samples with a medium Al-content suggest that the microstructure of the mixed oxide system changes drastically when the zinc content changes from 55 to 40% (see Figure 2). This change can be clearly seen in the TEM images of samples Zn40-c and Zn55-c (see parts e,f and g,h in Figure 6). In the images of Zn40-c two different types of areas can be found. There are aluminum-enriched areas (according to EDX data) that homogenously consist of small crystalline particles of spinel (ca. 5 nm, see Figure 6, f). In addition, there are zinc-enriched areas in which zinc oxide is clearly segregated from the spinel forming large crystals (>20 nm) of zincite resembling the crystals in Zn100-c (Figure 6, e). In contrast, images of Zn55-c show that this sample is nearly completely homogeneous (Figure 6, g), consisting of small spinel particles (≈5 nm) and some particles consisting of zincite. These particles may be needles or platelets seen in such a projection that they appear as needles. However, these needles are not segregated from the surrounding oxide matrix (Figure 6, h). In addition, these zincite needles do not resemble the crystals found in Zn100-c. The main difference is the crystallographic orientation of the needles. While the crystals in Zn100-c have a hexagonal base plate (a-b plane) and their longest dimension oriented parallel to the c-axis, the longest dimension of zincite needles in Zn55-c is orthogonally oriented to the c-axis. The needles have an average diameter of about 5 nm and may be more than 100 nm long. The lower specific surface area of Zn40-c compared to Zn55-c can be rationalized by the different dimensions of zincite crystals in these samples as the spinel particles of the samples are of comparable size.

In summary, phase composition and microstructural properties of calcined mixed oxide samples are influenced by the Zn/Al ratio. Samples with a Zn content higher than 55% contain only zincite as the detectable crystalline phase, while samples with a lower Zn content consist of ZnAl-spinel, zincite and alumina. A zinc content below 55% leads to inhomogeneous materials due to segregation of large zincite crystals. All results indicate the substitution of Al ions for Zn ions in zincite of zinc-rich samples.

Dried Precursor Samples

Dried precursor samples are investigated by XRD and thermogravimetric experiments (TG) coupled with evolved gas analysis (EGA) via on-line mass spectrometry (MS). The precursor materials are included in the investigation to gain a deeper understanding of the synthesis process and thus of the influence of the composition on the final mixed oxide samples.

The XRD patterns of the precursor materials in the state after drying overnight at 393 K are shown in Figure 7. The data of two PDF files assigned to carbonate-containing zinc minerals are included: hydrozincite $Zn_5(CO_3)_2(OH)_6 \cdot xH_2O$ and zaccagnaite $Zn_4Al_2[(OH)_{12}CO_3] \cdot 3H_2O$ (19–1458 and 38–0486, respectively). The composition of the dried precursor samples is strongly influenced by the nominal Zn/Al ratio. The identified phases include hydrozincite, zaccagnaite, boehmite, zincite, and ZnAl-spinel. Two intense reflections at $2\theta = 19.3°$ and $2\theta = 27.6°$ cannot be assigned to any known compound. Their presence indicates the formation of a further phase not yet described in the literature. As this phase is most probably a further hydroxy carbonate phase it is labeled phase HC in this contribution.

The pattern of the Al-free sample contains only reflections assignable to hydrozincite while the pattern of the Zn-free sample Zn00-d contains only broad reflections that can be assigned to boehmite AlO(OH). With exception of Zn98-d, hydrozincite can be found in all zinc-rich precursor samples with zinc contents above 85%. In the case of Zn98-d the phases formed during precipitation are already decomposed under the mild drying conditions applied (393 K, overnight) yielding single-phase zincite. This decomposition occurs partly during the drying of Zn96-d, too. Zn96-d contains zincite and hydrozincite. There are no indications for the presence of zincite in Zn92-d. Zn92-d contains zaccagnaite, hydrozincite, and small amounts of phase HC. While the reflections of zaccagnaite are intense and narrow, the reflections of hydrozincite and phase HC are weak and broad. Please note that in spite of its high intensity zaccagnaite can be only a minority species in Zn92-d due to the low Al-content of this sample. Zaccagnaite is present in nearly all Al-containing samples with exception of Zn98-d, Zn96-d, and Zn20-d. If present, the reflections of zaccagnaite are of similar intensity and width in all cases with exception of Zn55-d which contains only very small amounts of zaccagnaite. The intensity of the zaccagnaite reflections is influenced by many parameters. In addition to parameters correlated directly to sample preparation for XRD measurements, e.g. applied pressure when filling sample holders or sample mass, parameters like time elapsed between drying of the sample and XRD measurement also influence intensity of reflections in the case of zaccagnaite. This can be rationalized by the chemical memory effect described in the literature for hydrotalcite-like compounds.[55–57] Phase HC can be found to a larger extent in Zn85-d, Zn70-d, and Zn55-d. A closer comparison of the diffractograms regarding the range 2θ = 15–45° shows that Zn85-d, Zn70-d, and Zn55-d contain no significant amount of crystalline hydrozincite and thus that a reflection at about 2θ = 13° is part of the pattern of phase HC, too. No indications for the presence of phase HC are detected in the diffractograms of Zn40-d and Zn20-d. The diffractogram of Zn40-d exhibits in addition to the intense and narrow reflections of zaccagnaite several very broad and weak reflections that can be also found in the diffractogram of Zn20-d. By comparing the diffractograms of Zn20-d, Zn40-d, Zn20-c, and Zn40-c (Figure 1) these reflections can be clearly assigned to ZnAl-spinel. A close comparison of the diffractograms of Zn55-d and Zn55-c reveals that Zn55-d contains also low amounts of the oxidic species detectable in the calcined sample (zincite and ZnAl-spinel). The change in phase composition of dried precursor samples in the zinc-content range of 55 to 40% coincides with the change of the microstructure of calcined samples in this range. It can be speculated that the decomposition of phase HC leads to the homogeneous material containing long zincite needles that can be seen in the TEM images of Zn55-c (Figure 6, g) while the decomposition of aluminum-rich precursor material and zaccagnaite leads to segregation of large zincite crystals and small spinel particles.

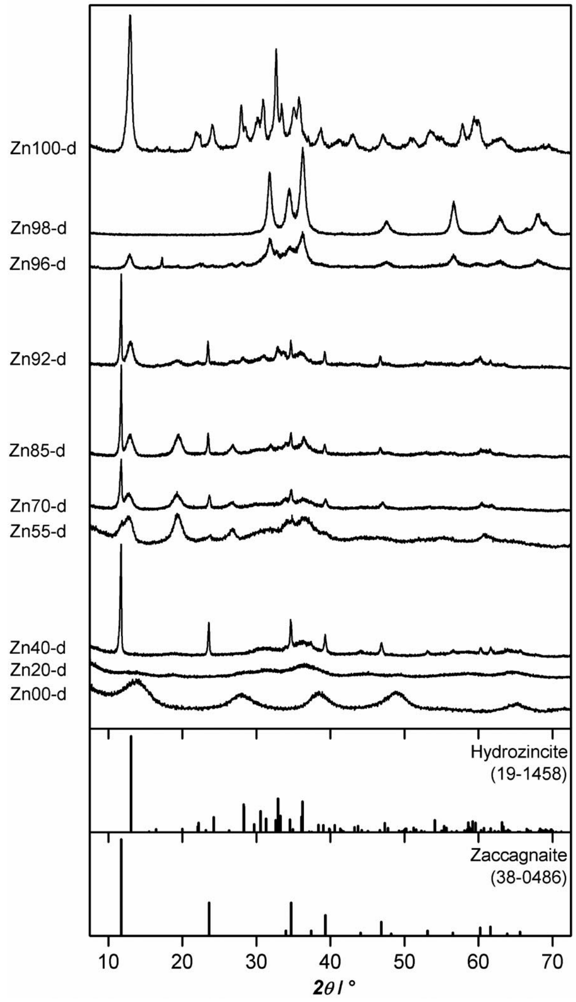

Figure 7. X-ray diffractograms of precursor samples in the state after drying overnight at 393 K. Patterns of hydrozincite $Zn_5(CO_3)_2(OH)_6\cdot xH_2O$ (PDF 19–1458) and zaccagnaite $Zn_4Al_2[(OH)_{12}CO_3]\cdot 3H_2O$ (PDF 38–0486) are included for comparison. Reflections at 2θ = 19.3° and 2θ = 27.6° are related to an unidentified compound.

The results of TG-MS experiments of the precursor samples in the state after drying at 393 K are shown in Figure 8. The light gray line corresponds to the differentiated mass loss (DTG signal) of the sample, the black line and dark gray lines show the ion currents of the masses m/z = 18 and m/z = 44 assignable to water and carbon dioxide, respectively. The ion currents are individually scaled to give a qualitative fit to the DTG signal. For all samples, no significant mass loss is observed above 750 K. The total mass loss measured over the whole temperature range of the experiments (300–1073 K) is also given in the figure. The total mass loss measured for all samples ranges between 16 and 27%, with exception of Zn98-d. According to the XRD data Zn98-d consists only of zincite after drying overnight at 398 K (Figure 7). The total mass loss of 2.5% measured for Zn98-d and the corresponding featureless DTG signal confirm this result. A comparison of the DTG signals shows that the introduction of aluminum leads to more amorphous materials. Peaks of the DTG signals become broader and less defined with increasing aluminum content. The MS traces of water and carbon dioxide both follow the trend of the DTG signal with increasing aluminum content. This indicates that physisorbed water is not the only reason for the broad DTG signals, but the carbonate species present in dried samples with high aluminum content are also in a highly disordered state. By combining the results of XRD and TG-MS experiments several peaks of the DTG signal can be directly related to separate phases. A peak at 500–505 K that is accompanied by simultaneous release of water and CO_2 can be assigned to the presence of hydrozincite. The TG-MS data indicates that small amounts of X-ray-amorphous hydrozincite are also present in the samples Zn85-d and Zn70-d which contain only phase HC and zaccagnaite as crystalline phases. A peak at 524–535 K that is also accompanied by simultaneous release of water and CO_2 can be directly related to the presence of phase HC thus confirming that phase HC is most probably a hydroxy carbonate phase. A peak at 411–437 K that is only due to release of water can be assigned to zaccagnaite. A peak around 450 K that is only due to release of water cannot be unambiguously assigned to any phase but may be related to sodium zinc carbonate. Samples containing zinc and aluminum give an additional release of CO_2 at temperatures above 550 K with exception of Zn98-d. There is no clear trend visible regarding the peak maximum temperature for this CO_2 release. The peak maximum temperature increases with increasing aluminum content until a maximum of 720 K in the case of Zn55-d is reached. For higher aluminum contents a peak maximum temperature cannot be determined properly as the MS traces of CO_2 become too broad and featureless. A decomposition step at elevated temperatures releasing only CO_2 is also described in the literature for dried precursors of copper catalysts prepared by coprecipitation.[51] It is related to the presence of so-called high-temperature carbonates. These high-temperature carbonates are found to positively influence the activity of copper catalysts for methanol synthesis. The change in phase composition observed in the XRD data of dried precursor samples in the zinc-content range of 55 to 40% is also reflected in the TG data. During calcination of aluminum-rich precursors the slow decomposition over a large temperature range seen in the TG experiments seems to favor the segregation process that leads to large zincite crystals while the defined decomposition of hydrozincite and phase HC during calcination of zinc-rich samples leads to homogeneous material without phase segregation.

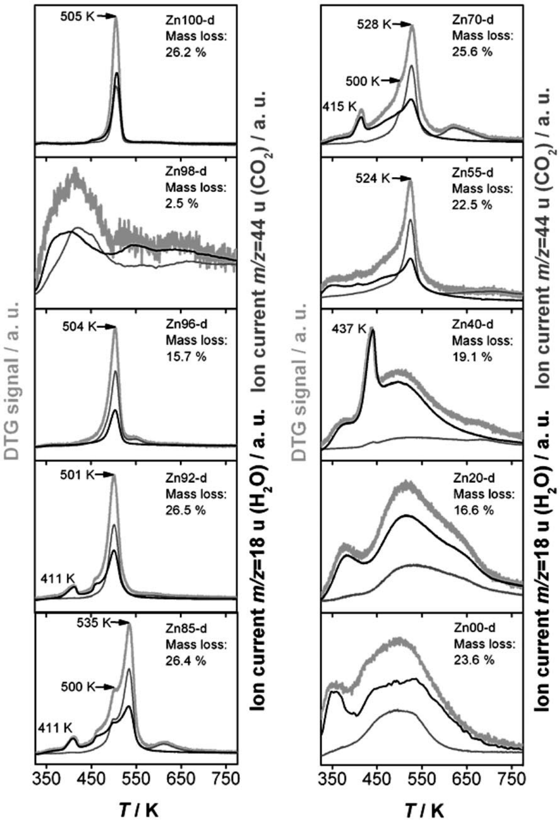

Figure 8. Results of TG experiments coupled with EGA of precursor samples in the state after drying at 393 K. The light gray line corresponds to the differentiated mass loss (DTG signal), black and dark gray lines show the MS traces assignable to water and carbon dioxide, respectively. For all samples, no significant mass loss is observed above 750 K. The total mass loss measured over the whole temperature range of 300–1073 K is also given in the figure.

In the case of several samples varied drying conditions are applied to investigate the processes occurring during the drying step. Separate batches of these samples are dried overnight at 393 K, dried overnight at 323 K, and freeze-dried. The XRD patterns of these precursor materials are shown in Figure 9. It is reported in the literature that under the applied preparation conditions sodium zinc carbonate is the main zinc-containing phase formed during precipitation.[27,58] By ageing the sodium zinc carbonate it is transformed into hydrozincite and sodium carbonate. As sodium carbonate is in contrast to sodium zinc carbonate or hydrozincite well soluble in water it is removed by washing. This result from the literature is reproduced in our study. Zn100-d contains nearly exclusively hydrozincite, regardless of the drying conditions. In the freeze-dried sample small amounts of sodium zinc carbonate can be detected. Drying at 323 K decomposes the sodium zinc carbonate partly, and drying at 393 K decomposes it completely. In contrast the hydrozincite in Zn100-d is not decomposed at these moderate temperatures. To rule out that an additional phase is the precursor of zincite in Zn98-d dried at 393 K, Zn98-d is also dried at 328 K. In the diffractogram of the sample dried at 328 K all reflections can be assigned to hydrozincite and sodium zinc carbonate and no indication of the presence of zincite can be found. Apparently small amounts of aluminum ions promote the decomposition of hydrozincite and sodium zinc carbonate at moderate temperatures. According to the diffractograms of Zn96-d and Zn92-d in Figure 7 higher amounts of aluminum seem to have a weaker or even no effect. Diffractograms of sample Zn55-d dried at 393 K, at 323 K, and freeze-dried can be compared to elucidate when phase HC is formed. It can be clearly seen that phase HC is already formed during precipitation or ageing and that phase HC is stable at temperatures up to

393 K. Crystalline zaccagnaite on the other hand is not present after ageing. It is formed during drying at 323 K, but decomposed by drying at 393 K. However, the decomposition during drying at 393 K is not irreversible. Reflections assignable to zaccagnaite can be found in the diffractogram of samples in the state after drying at 393 K if the samples are exposed to air for some time prior to the XRD measurement (Figure 7).

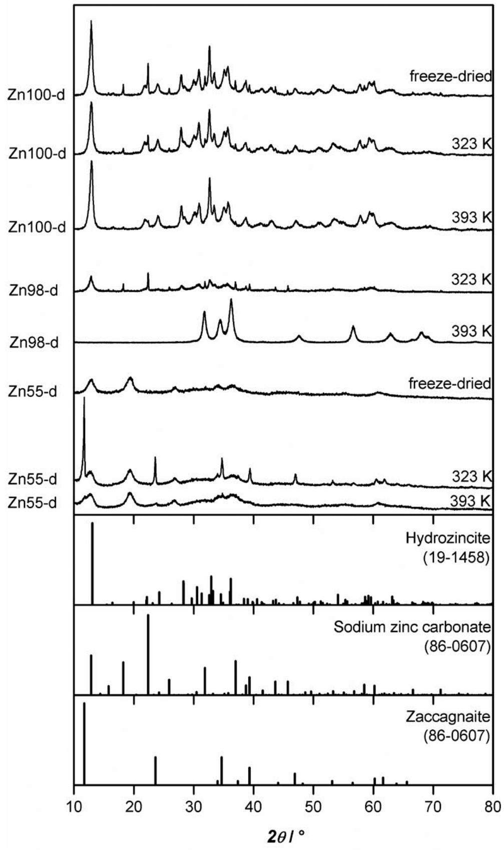

Figure 9. X-ray diffractograms of Zn100-d, Zn98-d, and Zn55-d in the state after various drying conditions (freeze-dried, overnight at 323 K, and overnight at 393 K). Patterns of hydrozincite $Zn_5(CO_3)_2(OH)_6\cdot xH_2O$ (PDF 19–1458), sodium zinc carbonate $Na_2Zn_3(CO_3)_4\cdot H_2O$ (PDF 86–0607), and zaccagnaite $Zn_4Al_2[(OH)_{12}CO_3]\cdot 3H_2O$ (PDF 38–0486) are included for comparison.

A comparison of experimental data of calcined and dried samples shows that zincite is formed during the calcination by the decomposition of hydrozincite and phase HC. Phase HC is a hydroxy carbonate phase not yet described in the literature. The decomposition of zaccagnaite may lead to zincite and either amorphous alumina or incorporation of Al^{3+} ions into zincite. A direct formation of spinel by decomposition of zaccagnaite seems improbable as zaccagnaite can be found in the precursor material of spinel-free samples and the Zn/Al ratio in zaccagnaite differs strongly from the ratio in spinel. It can be speculated that in aluminum-rich precursor material zaccagnaite reacts already at moderate temperatures with X-ray-amorphous aluminum species to form spinel.

Conclusions

The crystalline phases in precursor materials obtained by coprecipitation, ageing, and drying include hydrozincite, zaccagnaite, and an unknown hydroxy carbonate phase not yet described in the literature.

The thermal decomposition of hydrozincite and the unknown phase results in the formation of homogeneous zinc oxide material. It can be speculated that zaccagnaite reacts with X-ray-amorphous aluminum species yielding spinel.

It is found that the phase composition of calcined mixed oxide samples is influenced by the Zn/Al ratio in the used starting material solution. A Zn content higher than 55% leads to the formation of zincite only as the crystalline phase. A Zn content below 55% leads to the formation of ZnAl-spinel, zincite, and alumina.

Al ions substitute for Zn ions in zincite of zinc-rich samples. The substitution leads to a decrease of the volume of the unit cell of zincite.

With increasing aluminum content precursor materials become less crystalline, the mean diameter of crystallites in calcined samples decreases, and the specific surface area of calcined mixed oxides increases. In the zinc-content range of 55 to 40% the microstructure of calcined mixed oxides changes leading to an intermediate loss of specific surface area due to segregation of large zincite crystals.

Industrial $Cu/ZnO/Al_2O_3$ catalysts contain only small amounts of Al (<10%). It can be speculated that the substitution of Al ions for Zn ions reported in this contribution also occurs during the preparation of industrial catalysts. Therefore, aluminum might be more than a mere structural promoter for small metallic copper particles within this catalyst system.

Experimental Section

Samples with different Zn/Al ratios were prepared by coprecipitation at constant pH. Aqueous solutions (1.5 $mol\,L^{-1}$) of $Zn(NO_3)_2\cdot 6H_2O$ (Aldrich, 99.999%) and $Al(NO_3)_3\cdot 9H_2O$ (Aldrich, 99.997%) were premixed. The mixed solution was injected at a constant rate of 1.5 mL into a stirred tank reactor filled with 50 mL of HPLC-grade water that was thermostatted at 338 K. Simultaneously an aqueous solution of Na_2CO_3 (1.5 $mol\,L^{-1}$, Aldrich, 99.995%) was added to maintain the pH at a constant level of 7. After precipitation the precipitate was aged for 120 min under continuous stirring at the precipitation temperature. Afterwards, the precipitate was filtered and washed with water (six times, 10 mL). Finally, samples were dried overnight at 393 K in standing air and calcined at 593 K for 6 h in flowing synthetic air. In the case of a few samples drying conditions were varied to test the influence on the precursor material.

X-ray powder diffraction measurements were carried out to characterize the phase composition of the precursor and calcined samples, to determine lattice parameters of zincite and ZnAl-spinel and to analyze crystallite size and microstrain of zincite in zinc-rich specimens. Diffraction patterns were recorded in reflection geometry with a Panalytical MPD diffractometer, equipped with a copper tube, 0.5° divergent and antiscatter slits, a 0.2-mm high receiving slit, incident and diffracted beam 0.04 rad soller slits, and a secondary graphite monochromator. For qualitative phase analysis and lattice parameter refinements the specimens were scanned in the 5–(15)–100° 2θ range with a step width of 0.03° and 20–32 s/step collection time at an ambient temperature of $T = 300 \pm 2$ K. 9–20 wt.-% of an internal line standard (*F*-phlogopite NIST-SRM 675 in case of zincite and silicon SRM 640a in case of spinel) were added to samples for lattice parameter determinations. The ICDD powder diffraction file (PDF2) in conjunction with the X′Pert Line software (Panalytical, Almelo) was used for qualitative phase analysis. Line parameters ($K_\alpha 1$ position and intensity at peak maximum, FWHM, integral breadth β, asymmetry and pseudo-Voigt shape factor) of zincite and the internal standard were refined with the Profit line-fit software (Panalytical) assuming a fixed, pre-determined $K_\alpha 1/\alpha 2$ intensity ratio. The lattice parameters a and c of hexagonal zincite were calculated and refined with the least-squares program UnitCell[59] from 9 to 11 indexed diffraction lines, corrected for line shift due to geometric aberrations. The wavelength used in the calculations was $\lambda = 0.15406$ nm. Lattice parameters of Zn-Al-spinel in samples Zn20-c, Zn40-c, and Zn55-c were determined from Le Bail-type fits (GSAS Rietveld software[60]), in which line shape parameters (*GU*, *GV*, *GW*, *LX*, *LX* with function type 3) and lattice parameters were individually refined for each phase (except the lattice parameter of the silicon line standard, a = 0.5430825 nm), while global line shape (*S*/*L*, *H*/*L*) and geometrical parameters (trans, shift) were constrained to the same values in all phases (spinel, zincite, silicon line standard).

Three zincite specimens (Zn100-c, Zn98-c, Zn96-c) appeared to be suitable for diffraction line broadening analysis. These were scanned from 18 to 130° 2θ employing a diffracted beam 0.02 rad soller slit to reduce peak-shape asymmetry at $2\theta < 40°$ and enhance angular resolution. To ensure a similar peak-to-background ratio in all samples, step widths and collection times of measurements were varied from 0.030° to 0.040° and 30–90 s/step in the 18–44° 2θ range; 0.035° to 0.040° and 50–160 s/step in the 44–86° 2θ range; and 0.040° to 0.045° and 70–170 s/step in the 86–130° 2θ range. Line shape parameters were obtained from single-line fits with the Profit software (see above). Lanthanum hexaboride NIST-SRM 660a was used to correct for instrumental line broadening. We applied the integral-breadth method[33,41] to characterize the zincite samples microstructurally.

Static nitrogen physisorption experiments were performed in an Autosorb-1C setup (Quantachrome). Prior to the measurements, samples were degassed for 2 h under dynamic vacuum conditions at 473 K. Data were analyzed according to the BET equation, assuming the area covered by an N_2 molecule equals 0.162 nm^2.

Thermogravimetric analyses of coprecipitated precursor samples were conducted in a Cahn TG-131 thermobalance in a controlled flow of a mixture of 20% O_2 in He. Samples of about 70 mg were heated in open quartz crucibles from room temperature to 1073 K with a heating rate of 2 K min^{-1}. Evolved gases were monitored using a quadrupole mass spectrometer (QMS 200 Omnistar, Balzers) coupled to the thermal balance via a quartz capillary heated to 453 K.

One-dimensional ^{27}Al MAS NMR spectra were measured with a Bruker ASX400 spectrometer operating at a frequency of 104.27 MHz and a spinning speed of 30 kHz.

A Philips CM200FEG microscope operated at 200 kV and equipped with an EDX spectrometer (EDAX) was used for TEM investigations. The coefficient of spherical aberration was *Cs* = 1.35 mm. The information limit was better than 0.18 nm allowing the principal phases to be identified in HRTEM images. High-resolution images with a pixel size of 0.016 nm were taken at the magnification of 1083000 × with a CCD camera. Ni grids covered with 5-nm thick holey amorphous carbon film were used for specimen preparation. No liquids were used.

Acknowledgments

Financial support by the Bundesministerium für Bildung und Forschung (BMBF) in the scope of the project 01RI05028 (Entwicklung von Methanolsynthesekatalysatoren als Basis für nachhaltige Ressourcennutzung) is gratefully acknowledged.

---

[1] E. A. Meulenkamp, *J. Phys. Chem. B* **1998**, *102*, 5566–5572.
[2] V. Ischenko, S. Polarz, D. Grote, V. Stavarache, K. Fink, M. Driess, *Adv. Funct. Mater.* **2005**, *15*, 1945–1954.
[3] K. C. Waugh, *Catal. Today* **1992**, *15*, 51–75.
[4] H. H. Kung, *Catal. Rev. Sci. Eng.* **1980**, *22*, 235–259.
[5] H. Y. Chen, S. P. Lau, L. Chen, J. Lin, C. H. A. Huan, K. L. Tan, J. S. Pan, *Appl. Surf. Sci.* **1999**, *152*, 193–199.
[6] T. Fujitani, J. Nakamura, *Catal. Lett.* **1998**, *56*, 119–124.
[7] M. Kurtz, J. Strunk, O. Hinrichsen, M. Muhler, K. Fink, B. Meyer, C. Wöll, *Angew. Chem. Int. Ed.* **2005**, *44*, 2790–2794.
[8] H. Wilmer, M. Kurtz, K. V. Klementiev, O. P. Tkachenko, W. Grünert, O. Hinrichsen, A. Birkner, S. Rabe, K. Merz, M. Driess, C. Wöll, M. Muhler, *Phys. Chem. Chem. Phys.* **2003**, *5*, 4736–4742.
[9] M. M. Günter, T. Ressler, B. Bems, C. Büscher, T. Genger, O. Hinrichsen, M. Muhler, R. Schlögl, *Catal. Lett.* **2001**, *71*, 37–44.
[10] S. A. French, A. A. Sokol, S. T. Bromley, C. R. A. Catlow, S. C. Rogers, F. King, P. Sherwood, *Angew. Chem. Int. Ed.* **2001**, *40*, 4437–4440.
[11] S. A. French, A. A. Sokol, S. T. Bromley, C. R. A. Catlow, P. Sherwood, *Top. Catal.* **2003**, *24*, 161–172.
[12] J. C. Lavalley, J. Saussey, T. Rais, *J. Mol. Catal.* **1982**, *17*, 289–298.
[13] S. Polarz, J. Strunk, V. Ischenko, M. W. E. van den Berg, O. Hinrichsen, M. Muhler, M. Driess, *Angew. Chem. Int. Ed.* **2006**, *45*, 2965–2969.
[14] K. Fink, *Phys. Chem. Chem. Phys.* **2006**, *8*, 1482–1489.
[15] P. Lindan, E. Duplock, C. J. Zhang, M. Thomas, R. Chatten, A. Chadwick, *Dalton Trans.* **2004**, *19*, 3076–3084.
[16] J. Maier, *Phys. Chem. Chem. Phys.* **2003**, *5*, 2164–2173.
[17] J. C. H. Spence, *Science* **2003**, *299*, 839–841.
[18] P. Knauth, *J. Solid State Electrochem.* **2002**, *6*, 165–171.
[19] A. F. Kohan, G. Ceder, D. Morgan, C. G. Van de Walle, *Phys. Rev. B* **2000**, *61*, 15019–15027.
[20] K. Vanheusden, W. L. Warren, C. H. Seager, D. R. Tallant, J. A. Voigt, B. E. Gnade, *J. Appl. Phys.* **1996**, *79*, 7983–7990.
[21] D. C. Look, D. C. Reynolds, C. W. Litton, R. L. Jones, D. B. Eason, G. Cantwell, *Appl. Phys. Lett.* **2002**, *81*, 1830–1832.
[22] J. U. Brehm, M. Winterer, H. Hahn, *J. Appl. Phys.* **2006**, *100*, 064311.
[23] N. Y. Garces, L. Wang, L. Bai, N. C. Giles, L. E. Halliburton, G. Cantwell, *Appl. Phys. Lett.* **2002**, *81*, 622–624.
[24] D. Block, A. Hervé, R. T. Cox, *Phys. Rev. B* **1982**, *25*, 6049–6052.
[25] C. Gonzalez, D. Block, R. T. Cox, A. Hervé, *J. Cryst. Growth* **1982**, *59*, 357–362.
[26] B. Bems, M. Schur, A. Dassenoy, H. Junkes, D. Herein, R. Schlögl, *Chem. Eur. J.* **2003**, *9*, 2039–2052.
[27] S. Fujita, A. M. Satriyo, G. C. Shen, N. Takezawa, *Catal. Lett.* **1995**, *34*, 85–92.
[28] M. Kurtz, H. Wilmer, T. Genger, O. Hinrichsen, M. Muhler, *Catal. Lett.* **2003**, *86*, 77–80.
[29] H. Wilmer, T. Genger, H. Hinrichsen, *J. Catal.* **2003**, *215*, 188–198.
[30] R. Naumann d'Alnoncourt, M. Bergmann, J. Strunk, E. Löffler, O. Hinrichsen, M. Muhler, *Thermochim. Acta* **2005**, *434*, 132–139.

[31] R. Naumann d'Alnoncourt, X. Xia, J. Strunk, E. Löffler, O. Hinrichsen, M. Muhler, *Phys. Chem. Chem. Phys.* **2006**, *8*, 1525–1538.
[32] S. Kaluza, M. K. Schröter, R. Naumann d'Alnoncourt, T. Reinecke, M. Muhler, *Adv. Funct. Mater.* **2008**, *18*, 3670–3677.
[33] J. I. Langford, A. Boultif, J. P. Auffrédic, D. Louër, *J. Appl. Crystallogr.* **1993**, *26*, 22–33.
[34] P. Henderson, *Inorganic Geochemistry*, Pergamon Press, Oxford, **1982**.
[35] R. Hansson, P. C. Hayes, E. Jak, *Metall. Mater. Trans. B* **2004**, *35*, 633–642.
[36] R. Hansson, P. C. Hayes, E. Jak, *Can. Metall. Q.* **2005**, *44*, 111–118.
[37] S. Ghose, *Acta Crystallogr.* **1964**, *17*, 1051–1057.
[38] H. St. C. O'Neill, W. A. Dollase, *Phys. Chem. Miner.* **1994**, *20*, 541–555.
[39] S. J. Zinkle, G. P. Pells, *J. Nucl. Mater.* **1998**, *253*, 120–132.
[40] V. Perebeinos, S.-W. Chan, F. Zang, *Solid State Commun.* **2002**, *123*, 295–297.
[41] J. I. Langford, *NIST Spec. Publ.* **1992**, *846*, 110–126.
[42] N. Audebrand, J. P. Auffrédic, D. Louër, *Chem. Mater.* **1998**, *10*, 2450–2461.
[43] D. Louër, J. P. Auffrédic, J. I. Langford, D. Ciosmak, J. C. Niepce, *J. Appl. Crystallogr.* **1983**, *16*, 183–191.
[44] J. I. Langford, R. Delhez, Th. H. de Keijser, E. J. Mittemeijer, *Aust. J. Phys.* **1988**, *41*, 173–187.
[45] R. Vargas, D. Louër, J. I. Langford, *J. Appl. Crystallogr.* **1983**, *16*, 512–516.
[46] J. I. Langford, D. Louër, E. J. Sonneveld, J. W. Visser, *Powder Diffraction* **1986**, *1*, 211–221.
[47] O. García-Martínez, R. M. Rojas, E. Vila, *Solid State Ionics* **1993**, *63–65*, 442–449.
[48] N. Nava, P. Salas, M. E. Llanos, H. Perez-Pastenes, T. Viveros, *Hyperfine Interact.* **2005**, *161*, 11–19.
[49] J. J. Fripiat, L. J. Alvarez, J. S. Sánchez, E. M. Morales, J. M. Saniger, N. A. Sánchez, *Appl. Catal. A* **2001**, *215*, 91–100.
[50] C. Pecharromán, I. Sobrados, J. E. Iglesias, T. Gonzalez-Carreño, J. Sanz, *J. Phys. Chem. B* **1999**, *103*, 6160–6170.
[51] A. P. M. Kentgens, *Geoderma* **1997**, *80*, 271–306.
[52] N. J. van der Laag, M. D. Snel, P. C. M. M. Magusin, G. de With, *J. Eur. Ceram. Soc.* **2004**, *24*, 2417–2424.
[53] S. Lucchesi, A. Della Giusta, U. Russo, *Mineral. Magn.* **1998**, *62*, 41–54.
[54] S. V. Tsybulya, L. P. Solov'eva, L. M. Plyasova, O. P. Krivoruchko, *J. Struct. Chem.* **1991**, *32*, 386–388.
[55] A. E. Palomares, J. G. Prato, F. Rey, A. Corma, *J. Catal.* **2004**, *221*, 62–66.
[56] F. Cavani, F. Trifirò, A. Vaccari, *Catal. Today* **1991**, *11*, 173–301.
[57] M. Schur, B. Bems, A. Dassenoy, I. Kassatkine, J. Urban, H. Wilmer, O. Hinrichsen, M. Muhler, R. Schlögl, *Angew. Chem. Int. Ed.* **2003**, *42*, 3815–3817.
[58] T. E. Gier, X. Bu, S.-L. Wang, G. D. Stucky, *J. Am. Chem. Soc.* **1996**, *118*, 3039–3040.
[59] T. J. B. Holland, S. A. T. Redfern, *Min. Magn.* **1997**, *61*, 65–77.
[60] A. C. Larson, R. B. van Dreele, *GSAS – General Structure Analysis System*, LANSCE, MS-H805, Los Alamos National Laboratory, Los Alamos, NM, **2001**.

Received: October 7, 2008